

Crystal Structure Prediction and Phase Stability in Highly Anharmonic Silver-Based Chalcohalide Anti-Perovskites

Pol Benítez,^{1,2} Cibrán López,^{1,2} Cong Liu,³ Ivan Caño,^{2,4}
Josep-Lluís Tamarit,^{1,2} Edgardo Saucedo,^{2,4} and Claudio Cazorla^{1,2}

¹*Group of Characterization of Materials, Departament de Física,
Universitat Politècnica de Catalunya, Campus Diagonal-Besòs,
Av. Eduard Maristany 10-14, 08019 Barcelona, Spain*

²*Research Center in Multiscale Science and Engineering,
Universitat Politècnica de Catalunya, Campus Diagonal-Besòs,
Av. Eduard Maristany 10-14, 08019 Barcelona, Spain*

³*Departament de Física, Universitat Politècnica de Catalunya,
Campus Nord, Jordi Girona 1-3, 08005 Barcelona, Spain*

⁴*Department of Electronic Engineering, Universitat Politècnica de Catalunya, 08034 Barcelona, Spain*

Silver-based chalcohalide anti-perovskites (CAP), Ag_3BC ($\text{B} = \text{S}, \text{Se}; \text{C} = \text{Cl}, \text{Br}, \text{I}$), represent an emerging family of energy materials with intriguing optoelectronic, vibrational and ionic transport properties. However, the structural features and phase stability of CAP remain poorly investigated to date, hindering their fundamental understanding and potential integration into technological applications. Here we employ theoretical first-principles methods based on density functional theory to fill this knowledge gap. Through crystal structure prediction techniques, *ab initio* molecular dynamics simulations, and quasi-harmonic free energy calculations, we unveil a series of previously overlooked energetically competitive phases and temperature-induced phase transitions for all CAP. Specifically, we identify a new cubic $P2_13$ structure as the stable phase of all CAP containing S both at zero temperature and $T \neq 0$ K conditions. Consequently, our calculations suggest that the cubic $Pm\bar{3}m$ phase identified in room-temperature X-ray diffraction experiments is likely to be metastable. Furthermore, for CAP containing Se, we propose different orthorhombic ($Pca2_1$ and $P2_12_12_1$) and cubic ($I2_13$) structures as the ground-state phases and reveal several phase transformations induced by temperature. This theoretical investigation not only identifies new candidate ground-state phases and solid-solid phase transformations for all CAP but also provides insights into potential stability issues affecting these highly anharmonic superionic materials.

I. INTRODUCTION

Silver-based chalcohalide anti-perovskites (CAP) with chemical formula Ag_3BC ($\text{B} = \text{S}, \text{Se}; \text{C} = \text{Cl}, \text{Br}, \text{I}$) are structurally similar to the lead halide perovskites (e.g., CsPbI_3), with the “anti” designation indicating the exchange of anions and cations compared to the typical ionic perovskite arrangement. Analogous to lead halide perovskites, CAP are highly promising materials for energy and optoelectronic applications, boasting low toxicity due to their lead-free composition [1, 2]. The two most extensively studied CAP compounds, Ag_3SBr and Ag_3SI , possess experimentally determined band gaps of approximately 1.0 eV [3, 4], rendering them favorable for photovoltaic applications. These have been also recognized as room-temperature superionic conductors [5, 6]. Owing to their substantial vibrational anharmonicity and intriguing transport properties [7, 8], CAP have been also investigated as potential thermoelectric materials [9, 10].

The current surge in interest in CAP is evident from the recent publication of several experimental works detailing improved synthesis methods. The pioneering synthesis of the archetypal CAP Ag_3SI and Ag_3SBr dates back to 1960, credited to Reuter and Hardel [11]. However, the majority of early CAP synthesis techniques required vacuum conditions, elevated temperatures (> 600 K), and prolonged synthesis durations, often span-

ning during days or even months. More recently, rapid synthesis routes have emerged, enabling the production of high-purity Ag_3SI and Ag_3SBr powders at temperatures below 600 K through mechanochemistry methods [3]. Furthermore, advancements have also led to the synthesis of CAP solid solutions, such as $\text{Ag}_3\text{SBr}_x\text{I}_{1-x}$ ($0 \leq x \leq 1$), employing a rapid solution-based chemical approach at moderate temperatures (< 500 K) [4].

Despite these recent experimental advances in synthesis, the phase stability and structural properties of CAP remain inadequately investigated and understood to date. For both Ag_3SBr and Ag_3SI , three distinct polymorphs have been consistently reported: a low-temperature γ phase (< 130 – 160 K), a room-temperature phase denoted as β with low ionic conductivity, and an α phase at high temperatures (> 500 K) exhibiting high ionic Ag^+ conductivity and S^-/I^- or S^-/Br^- chemical disorder [12–14]. Regarding Ag_3SCl and other CAP compounds containing Se, to the best of our knowledge, there is no experimental data available concerning their structural and phase stability properties.

In the original reports by Hoshino *et al.* [12–14], the low-temperature γ phase was described as trigonal with space group $R\bar{3}$ for Ag_3SI and orthorhombic with space group $Cmcm$ for Ag_3SBr . The room-temperature β phase for both Ag_3SI and Ag_3SBr was identified as cubic with space group $Pm\bar{3}m$ and the high-temperature

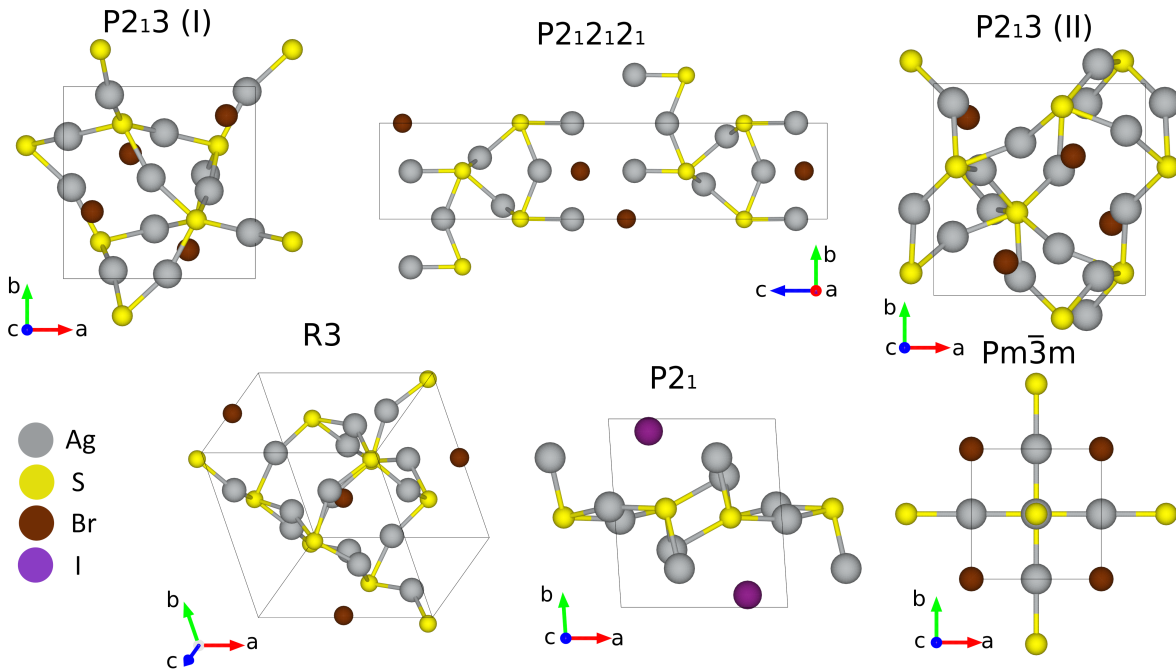


FIG. 1. Sketch of some energetically competitive crystal structures predicted with CSP-DFT methods for the archetypal silver-based chalcogenide anti-perovskites Ag_3SBr and Ag_3SI . The cubic $Pm\bar{3}m$ phase that has been experimentally identified as the corresponding room-temperature β phase is shown for comparison. Additional representations of other energetically competitive crystal structures are provided in the Supplementary Fig.1.

disordered α phase as cubic with space group $Im\bar{3}m$ [6, 15, 16]. Additionally, a metastable room-temperature phase exhibiting high ionic conductivity, denoted as α^* and obtained through quenching of the α phase, has been reported for Ag_3SI [6, 15]. However, subsequent studies on Ag_3SBr suggested that the crystal symmetry of the low-temperature γ phase could be more accurately described as monoclinic or triclinic, rather than orthorhombic [17]. Furthermore, investigations into several $\text{Ag}_3\text{SBr}_x\text{I}_{1-x}$ solid solutions revealed that for a range of mixed compositions, the low-temperature γ phase was orthorhombic with space group $Pnm2_1$ or $Pnmm$ [17].

Since all existing CAP synthesis methods involve temperatures above ambient conditions, temperatures at which Ag_3SI and Ag_3SBr exhibit ionic conductivity, it is highly probable that upon annealing the samples remain dynamically arrested in metastable states characterized by ionic disorder. This phenomenon is originated by the existence of significant energy barriers that hinder the transition towards energetically more favorable and ordered phases. A similar behavior has been recently demonstrated for halide hybrid perovskites [18]. This tendency poses a significant challenge in identifying truly stable low-temperature phases in CAP. Systematic studies able to precisely evaluate the relative stability among different CAP polymorphs are therefore urgently needed. Such investigations are crucial for improving our fundamental understanding of CAP and to properly assess their potential for possible technological applications.

In this study, we employ theoretical first-principles methods based on density functional theory to discern candidate stable phases for all CAP compounds at both zero-temperature and $T \neq 0$ conditions. Notably, the predicted lowest-energy CAP phases, systematically identified through crystal structure prediction, *ab initio* molecular dynamics, and quasi-harmonic free energy techniques, differ from those previously reported in experimental studies. Therefore, besides providing original and valuable data for Ag_3SBr and other CAP compounds containing Se, the present study prompts a reassessment of the established phase diagrams for Ag_3SI and Ag_3SBr , urging further experimental investigations into CAP.

II. RESULTS

A. Zero-temperature crystal structure prediction

We conducted zero-temperature crystal structure prediction (CSP) calculations for the two archetypal CAP compounds, Ag_3SBr and Ag_3SI , using the MAGUS software [19] and considering a maximum of 20 atoms per unit cell (Methods). MAGUS employs an evolutionary algorithm augmented with machine learning techniques and graph theory. The initial structures proposed by MAGUS were subsequently relaxed using first-principles methods based on density functional theory (DFT, Methods). Figure 1 illustrates some of the energetically most

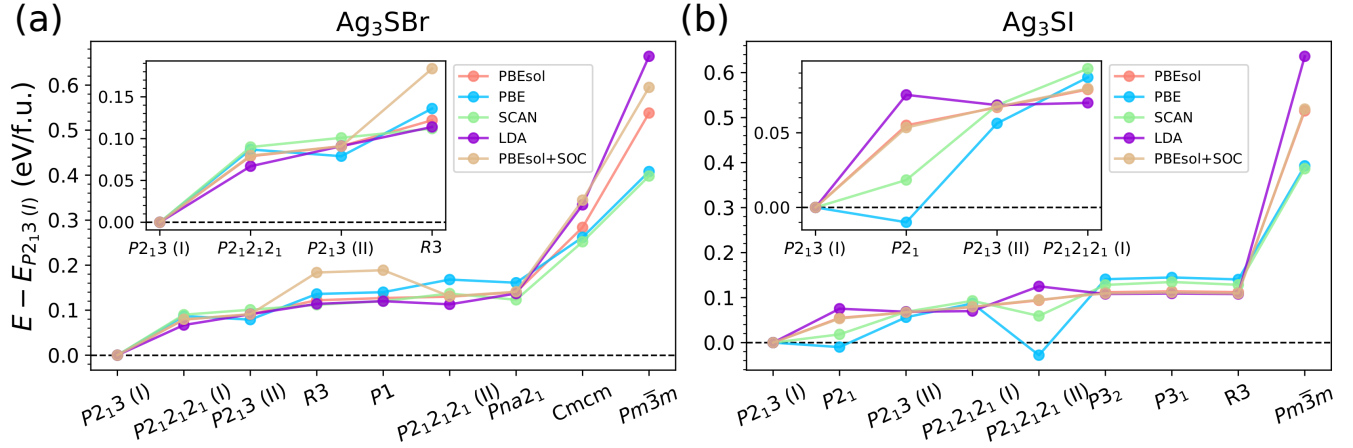


FIG. 2. Energy of competitive crystal structures calculated for archetypal CAP using different DFT exchange-correlation functionals. (a) Ag_3SBr and (b) Ag_3SI . The energy of the cubic $Pm\bar{3}m$ phase that is experimentally resolved at room temperature is shown for comparison.

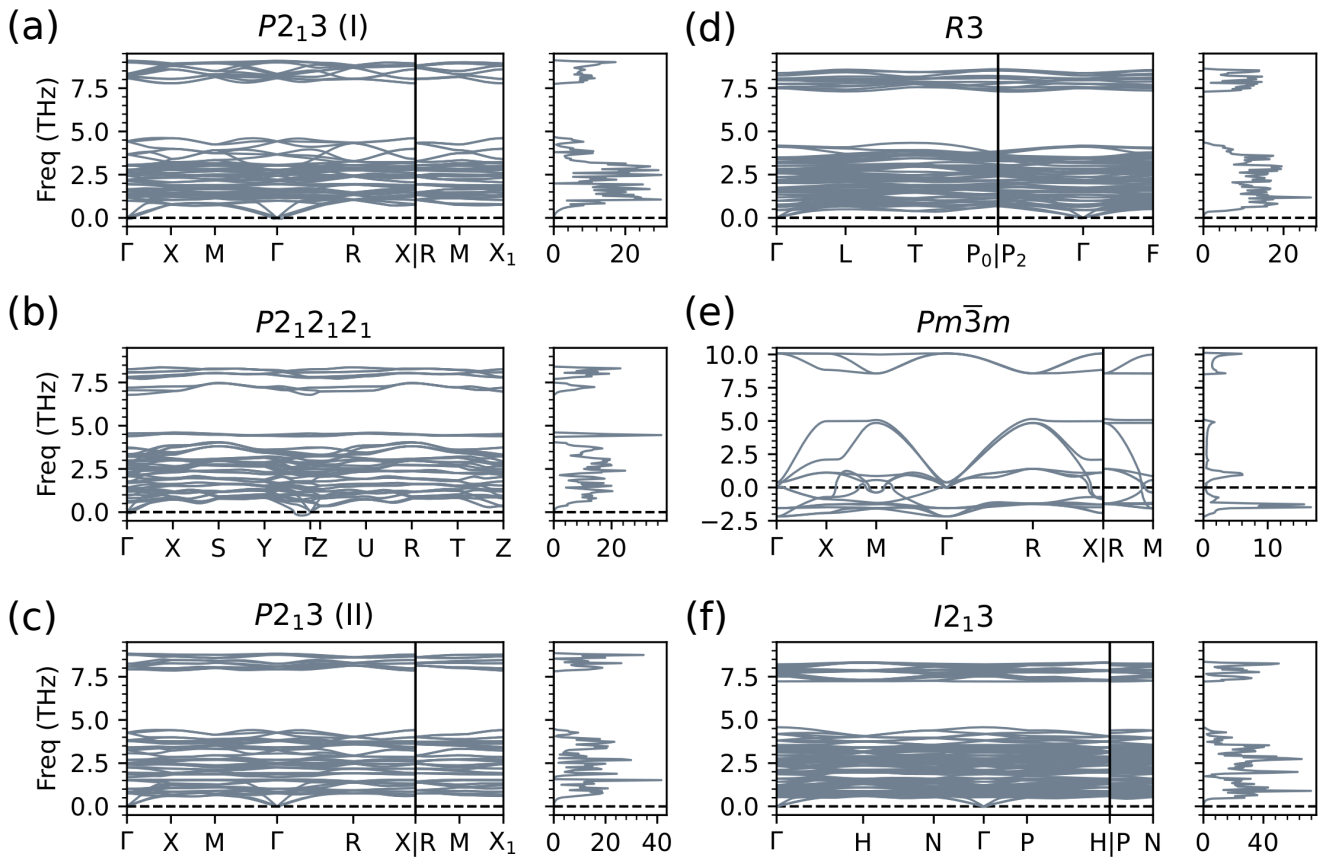


FIG. 3. Vibrational phonon spectrum of Ag_3SBr calculated for different crystal structures. Phonon calculations were performed at zero-temperature conditions. All considered phases are vibrationally stable made the exception of the cubic $Pm\bar{3}m$ phase, which exhibits abundant imaginary phonon frequencies and branches. Results were obtained with the semi-local functional PBEsol [22].

favorable phases identified in the rankings resulting from our CSP-DFT calculations (additional structural representations can be found in Supplementary Fig.1). Notable among them are two distinct cubic structures with space group $P2_13$, an orthorhombic $P2_12_12_1$ phase, a monoclinic $P2_1$ phase and a trigonal $R3$ phase.

Figure 2 presents the structure energy rankings obtained for Ag_3SBr and Ag_3SI using various DFT semilocal exchange-correlation energy functionals, including LDA [20], PBE [21], PBEsol [22] and SCAN [23]. For Ag_3SBr , all the examined DFT functionals consistently identify the cubic $P2_13$ (I) structure as the ground-state phase (Fig.2a). At $T = 0$ K conditions, the second energetically most favorable structure is an orthorhombic $P2_12_12_1$ phase, followed by a cubic $P2_13$ (II) and a trigonal $R3$ phase. Notably, the PBE functional is the sole functional predicting the cubic $P2_13$ (II) phase to be marginally more favorable than the orthorhombic $P2_12_12_1$ phase. Incorporating spin-orbit coupling (SOC) effects in the DFT calculations appears inconsequential for determining the most energetically competitive phases, as indicated by the similarity between the PBEsol and PBEsol+SOC curves.

Remarkably, our crystal CSP-DFT calculations do not classify the orthorhombic $Cmcm$ or the cubic $Pm\bar{3}m$ phases as energetically competitive, despite their proposal as the γ and β phases of Ag_3SBr from experiments [12–14]. Consistently, across all the examined DFT functionals, the energy of these two phases is several hundreds of meV per formula unit (f.u.) higher than that of the theoretical ground state, the cubic $P2_13$ (I) phase (Fig.2a).

For Ag_3SI , the energy ranking is also dominated by the cubic $P2_13$ (I) phase, closely followed by a monoclinic $P2_1$ phase (Fig.2b). However, the PBE functional deviates from the other energy functionals, suggesting an orthorhombic $P2_12_12_1$ phase as the ground state. In this case, accounting for SOC effects in the DFT calculations neither poses a significant variation in the energy difference results, as evidenced by the nearly identical curves for PBEsol and PBEsol+SOC. Another cubic $P2_13$ (II) phase emerges as energetically competitive across all surveyed DFT functionals.

Likewise to Ag_3SBr , the energy of the experimentally observed low-temperature trigonal $R3$ and room-temperature cubic $Pm\bar{3}m$ phases of Ag_3SI is estimated to be substantially higher than that of the corresponding ground-state phase (> 0.1 eV/f.u.) by all the examined functionals. It is worth noting the similarity in energy among the trigonal $P3_2$ and $P3_1$ phases identified in our CSP-DFT calculations and the experimentally identified trigonal $R3$ phase, which stems from their structural resemblance.

Figures 3–4 show the vibrational phonon spectra calculated for the four most energetically favorable structures determined for Ag_3SBr and Ag_3SI at zero temperature, respectively, along with those of the cubic $Pm\bar{3}m$ phase and another cubic $I2_13$ phase introduced in the next

section. Across the four predicted stable polymorphs, we observe no imaginary phonon frequencies along their high-symmetry reciprocal space paths, indicating their vibrational stability. Notably, all these phases exhibit a wide frequency band gap spanning approximately from 5.0 to 7.5 THz, with the exception of the orthorhombic $P2_12_12_1$ phase that displays slightly lower frequencies in the high-frequency regime.

Conversely, the cubic $Pm\bar{3}m$ phase, proposed as the room-temperature β phase of both Ag_3SBr and Ag_3SI [13, 14], exhibits numerous imaginary phonon frequencies along all high-symmetry reciprocal space paths, indicating its vibrational instability at $T = 0$ K conditions. A possible T -induced stabilization of this cubic $Pm\bar{3}m$ phase will be discussed further in Sec.III. Additionally, the orthorhombic $Cmcm$ phase, suggested as the low-temperature γ phase of Ag_3SBr [13, 14], exhibits also abundant imaginary phonon frequencies (Supplementary Fig.2). Consequently, this phase is vibrationally unstable at low temperatures and, even ignoring its highly unfavourable energy, cannot be regarded as the ground-state phase. On the contrary, the trigonal $R3$ phase, proposed as the low-temperature γ phase of Ag_3SI [13, 14], appears to be vibrationally stable at $T = 0$ K conditions (Supplementary Fig.2); however, in view of its high energy (Fig.2b), this phase should be regarded as metastable in the low-temperature regime.

As demonstrated in this section, our CSP-DFT calculations yield a significantly different set of candidate ground-state phases compared to those experimentally suggested for Ag_3SBr and Ag_3SI . Specifically, a cubic $P2_13$ phase consistently emerges as the most energetically favorable phase at low temperatures in our calculations, closely followed by an orthorhombic $P2_12_12_1$ and a monoclinic $P2_1$ phase, depending on the material. Importantly, these new candidate ground-state phases are all shown to be vibrationally stable, contrasting with, for example, the orthorhombic $Cmcm$ phase proposed as the lowest energy structure of Ag_3SBr . Consequently, our theoretical findings call for a reevaluation of previous experimental characterizations of CAP conducted at low temperatures.

B. Finite-temperature crystal structure prediction

The observed low-temperature vibrational instability of the cubic $Pm\bar{3}m$ phase (Figs.3–4), proposed as the room-temperature β phase of both Ag_3SBr and Ag_3SI [13, 14], prompted us to perform comprehensive *ab initio* molecular dynamics (AIMD) simulations at $T \neq 0$ K conditions (Methods). The primary objective of these dynamical simulations was to assess the vibrational stability of this phase at finite temperatures as well as to evaluate its ionic transport properties. All the results presented in what follows, if not stated otherwise, were obtained with the semilocal PBEsol exchange-correlation energy functional [22].

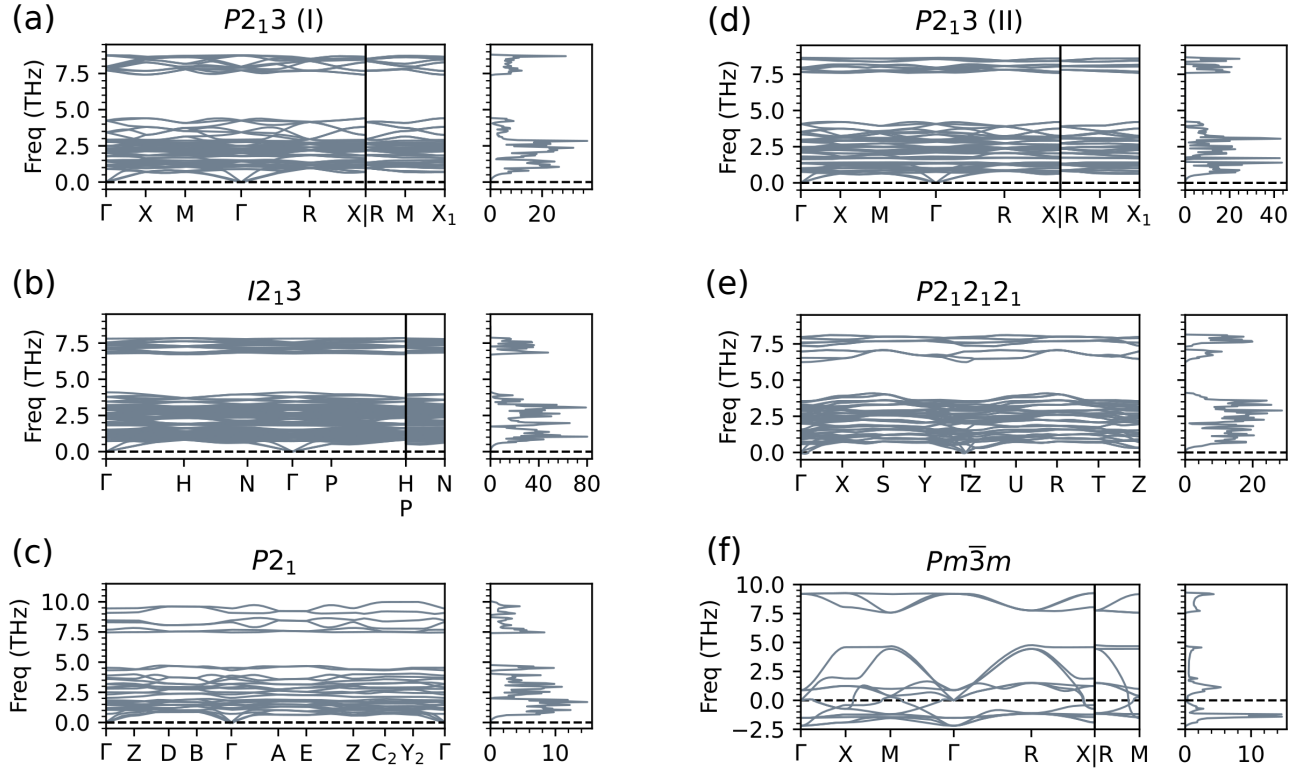


FIG. 4. **Vibrational phonon spectrum of Ag_3SI calculated for different crystal structures.** Phonon calculations were performed at zero-temperature conditions. All considered phases are vibrationally stable made the exception of the cubic $Pm\bar{3}m$ phase, which exhibits abundant imaginary phonon frequencies and branches. Results were obtained with the semi-local functional PBEsol [22].

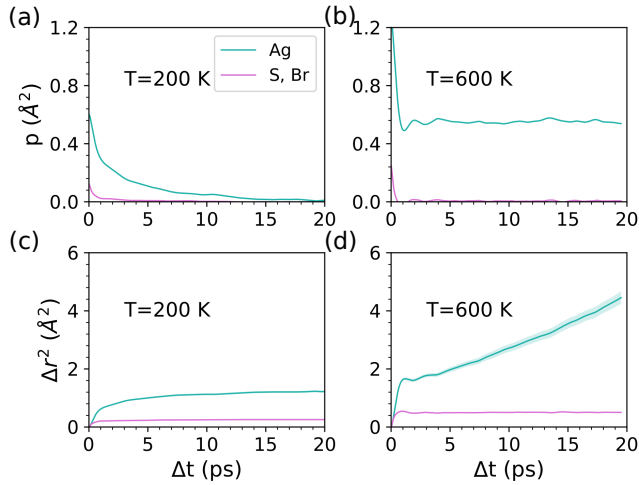


FIG. 5. **Analysis of the vibrational stability and ionic diffusion of Ag_3SBr in the cubic $Pm\bar{3}m$ phase at $T \neq 0$ conditions.** (a)–(b) Position correlation function [24, 25], $p(\Delta t)$, estimated at $T = 200$ and 600 K. (c)–(d) Mean square displacement, $\Delta r^2(\Delta t)$, estimated at $T = 200$ and 600 K. Results were obtained from *ab initio* molecular dynamics simulations (Methods) performed with the semi-local functional PBEsol [22].

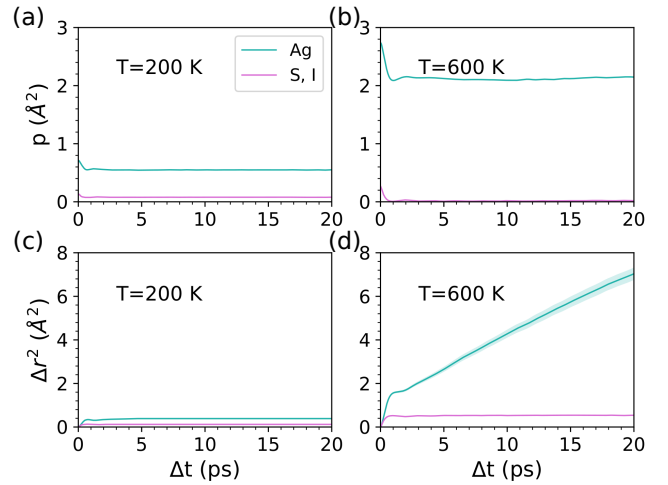


FIG. 6. **Analysis of the vibrational stability and ionic diffusion of Ag_3SI in the cubic $Pm\bar{3}m$ phase at $T \neq 0$ conditions.** (a)–(b) Position correlation function [24, 25], $p(\Delta t)$, estimated at $T = 200$ and 600 K. (c)–(d) Mean square displacement, $\Delta r^2(\Delta t)$, estimated at $T = 200$ and 600 K. Results were obtained from *ab initio* molecular dynamics simulations (Methods) performed with the semi-local functional PBEsol [22].

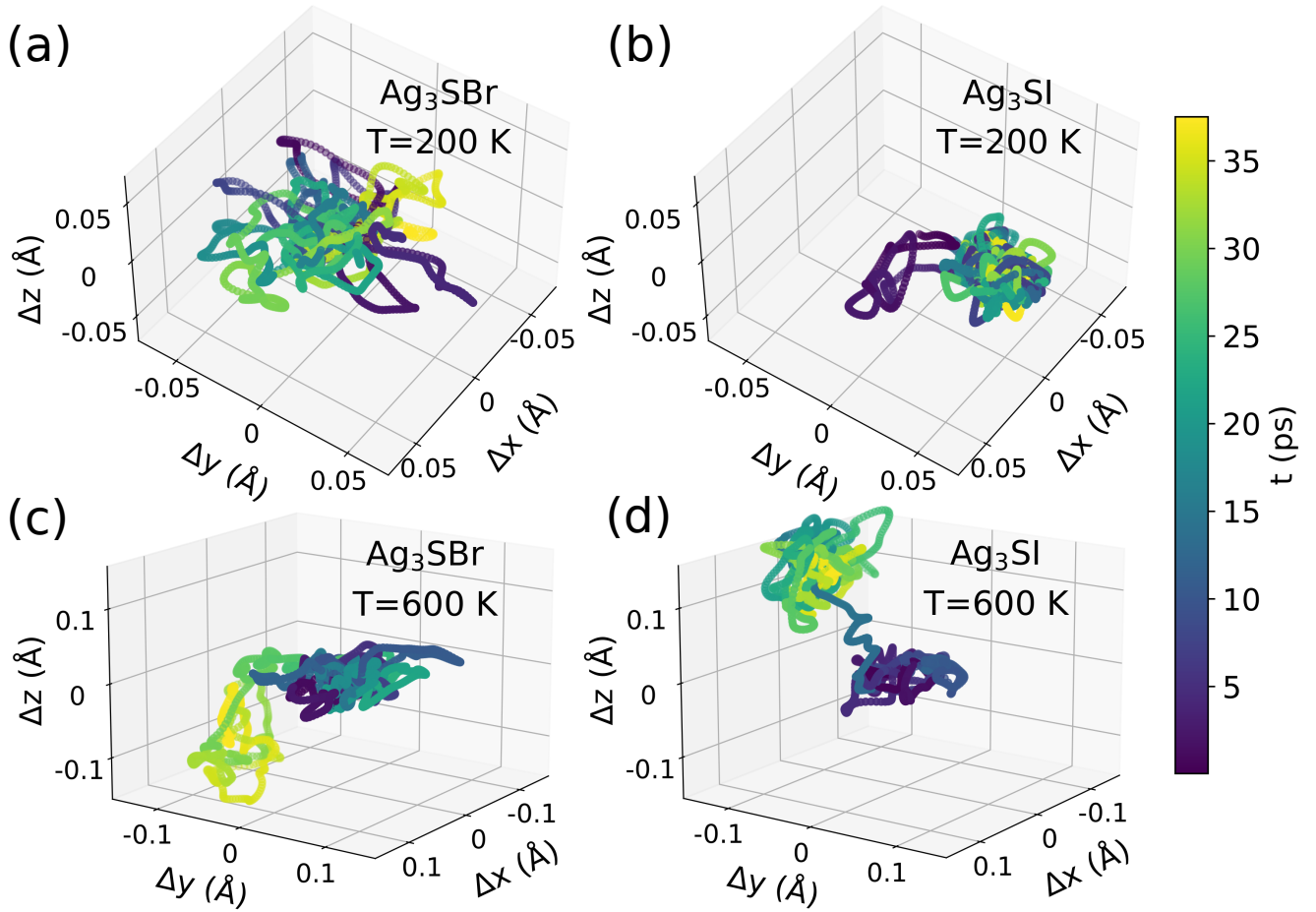


FIG. 7. Analysis of Ag ion trajectories obtained from *ab initio* molecular dynamics simulations. Ag₃SBr in the cubic $Pm\bar{3}m$ phase at (a) $T = 200$ K and (c) $T = 600$ K. Ag₃SI in the cubic $Pm\bar{3}m$ phase at (b) $T = 200$ K and (d) $T = 600$ K. Results were obtained with the semi-local functional PBEsol [22].

Figure 5 shows the position correlation function, $p(\Delta t)$, and mean square displacement, $\Delta r^2(\Delta t)$, estimated for Ag₃SBr at $T = 200$ and 600 K. These time-dependent functions are defined as [24, 25]:

$$p(\Delta t) = \langle [\mathbf{r}_i(\Delta t + t_0) - \mathbf{R}_i^0] \cdot [\mathbf{r}_i(t_0) - \mathbf{R}_i^0] \rangle \quad (1)$$

$$\Delta r^2(\Delta t) = \langle [\mathbf{r}_i(\Delta t + t_0) - \mathbf{r}_i(t_0)]^2 \rangle, \quad (2)$$

where \mathbf{r}_i represents the position vector of atom i , t_0 an arbitrary time origin, \mathbf{R}_i^0 the position vector of the equilibrium lattice site for atom i , and $\langle \dots \rangle$ thermal average performed over particles and time origins.

At $\Delta t = 0$, p is simply the vibrational mean square displacement. The crystal is vibrationally stable if $p(\Delta t \rightarrow \infty) = 0$, because the vibrational displacements at widely separated times become uncorrelated. Conversely, if the atoms acquire a permanent vibrational displacement, $p(\Delta t \rightarrow \infty)$ becomes nonzero. On the other hand, in the absence of ionic diffusion, Δr^2 converges to a constant equal to twice the vibrational mean square displacement in the limit $\Delta t \rightarrow \infty$. Contrarily, in the presence of ionic diffusion, Δr^2 exhibits a linear dependence on Δt with a

positively defined slope at sufficiently long times.

The p and Δr^2 results presented in Fig.5 indicate that Ag₃SBr in the cubic $Pm\bar{3}m$ phase is vibrationally stable at $T = 200$ K and exhibits significant Ag ionic diffusion at $T = 600$ K. The slow decay of p and large asymptotic value of Δr^2 estimated for Ag ions at $T = 200$ K indicate high anharmonicity, despite of the low temperature. In contrast, the p and Δr^2 results presented in Fig.6 indicate a markedly different behavior for Ag₃SI. Specifically, the vibrational centers of Ag ions somewhat change throughout the $T = 200$ K simulation, $\{\mathbf{R}_i^0\} \rightarrow \{\mathbf{R}_i^*\}$, since $p(\Delta t \rightarrow \infty) \neq 0$ for these atoms. Furthermore at high temperatures, the Ag ionic diffusion is appreciably higher in Ag₃SI than in Ag₃SBr.

Figure 7 shows the simulated trajectory of an arbitrary silver ion in Ag₃SBr and Ag₃SI at different temperatures. At $T = 200$ K, the map of position points is more anisotropic for Ag₃SI than for Ag₃SBr. Specifically, multiple vibrational centers can be identified for Ag₃SI (Fig.7b), whereas they are not observed for Ag₃SBr (Fig.7a). Notably, the amplitude of the ionic vibrations in Ag₃SBr is very wide, thus denoting high anharmonic-

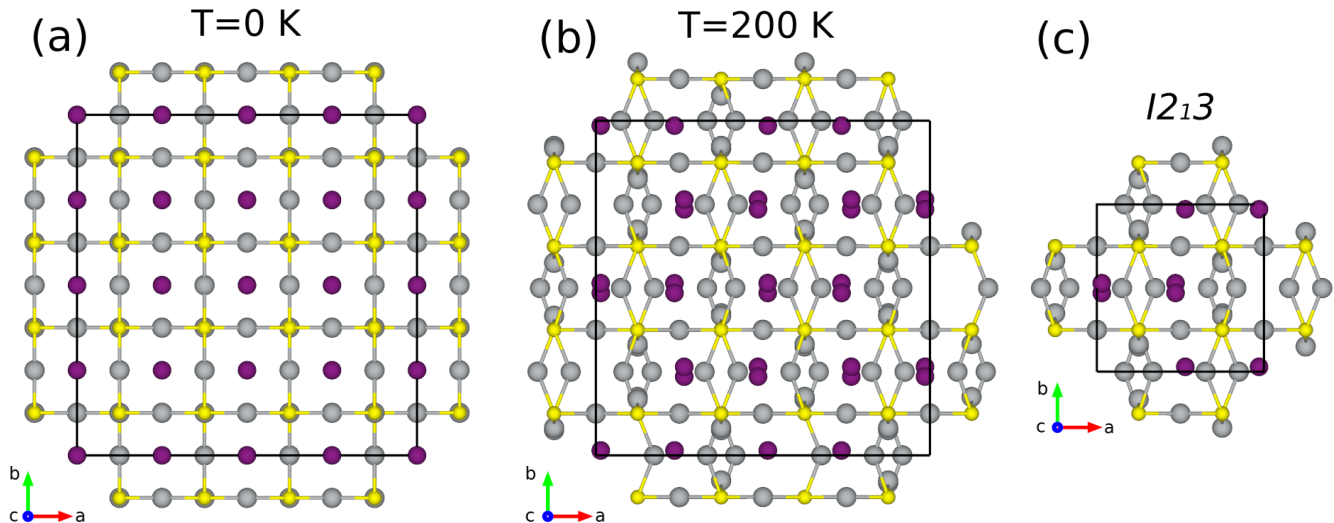


FIG. 8. Ag_3SI supercell representations obtained from *ab initio* molecular dynamics simulations. (a) The starting cubic $Pm\bar{3}m$ phase at zero temperature. (b) The distorted cubic $Pm\bar{3}m$ phase found at $T = 200$ K. (c) The new cubic $I2_13$ phase determined from the distorted cubic $Pm\bar{3}m$ phase. Ag, S and I ions are represented with grey, yellow and purple spheres, respectively. Results were obtained with the semi-local functional PBEsol [22].

ity. These observations are consistent with the p results presented in Figs.5–6 for Ag ions. At $T = 600$ K, on the other hand, silver ionic hoppings are clearly observed in both compounds, illustrating their superionic character at high temperatures.

In an attempt to identify the crystal structure towards which Ag_3SI appears to transform from the cubic $Pm\bar{3}m$ phase, we performed annealing (i.e., zero-temperature geometry relaxation) on a series of supercell configurations extracted from the AIMD runs (Fig.8). Figure 8b shows the lowest-energy configuration obtained through this process, which contains a total of 320 atoms. Using the FINDSYM software [26], this supercell was efficiently reduced to a cubic 40-atom primitive cell with space group $I2_13$ (Fig.8c). Interestingly, this new cubic $I2_13$ phase was found to be vibrationally stable at low temperatures for both Ag_3SBr and Ag_3SI (Figs.3–4). As discussed in the next section, this new cubic $I2_13$ phase was also found to be energetically competitive with respect to the ground-state phases determined for most silver chalcogenide anti-perovskite (CAP).

C. Zero-temperature phase competition

After the detailed study of the structural and vibrational properties of Ag_3SBr and Ag_3SI , we extended our investigation to other materials in the CAP family, namely, Ag_3SCl , Ag_3SeCl , Ag_3SeBr and Ag_3SeI . It is worth noting that, to the best of our knowledge, there are not experimental reports on these compounds in the literature. For each new CAP, we began by relaxing the 60 lowest-energy phases identified for the archety-

pal compounds Ag_3SBr and Ag_3SI , using the semi-local PBEsol exchange-correlation energy functional [22]. The cubic $I2_13$ phase discovered from the AIMD simulations performed for Ag_3SI and the experimental room-temperature cubic $Pm\bar{3}m$ phase, were additionally considered in our pool of candidate ground-state phases.

Figure 9 and Table I summarize our zero-temperature DFT structure energy rankings obtained for the CAP family. For Ag_3SBr and Ag_3SI , the primary difference compared to the results in Fig.2 is the inclusion of the new cubic $I2_13$ phase. This phase has an energy only 45 meV/f.u. higher than the cubic $P2_13$ (I) ground-state phase in Ag_3SI , and approximately 100 meV/f.u. higher than the same ground-state phase in Ag_3SBr . For the analogous Se-based CAP, the cubic $I2_13$ phase is even more relevant; it has the lowest energy for Ag_3SeI , and for Ag_3SeBr its energy is only about 35 meV/f.u. higher than that of the orthorhombic $P2_12_12_1$ ground-state phase (Fig.9).

The ground-state phase of all analyzed S-based CAP corresponds to the cubic $P2_13$ (I) phase, which in the Ag_3SCl system is closely followed by two orthorhombic phases with symmetries $P2_12_12_1$ and $Pca2_1$. Regarding the Se-based CAP, in Ag_3SeCl and Ag_3SeBr , the lowest-energy phases are dominated by orthorhombic phases (e.g., $P2_12_12_1$ and $Pca2_1$), the cubic $I2_13$ phase being the most significant energy competitor presenting a different crystal symmetry. In the specific case of Ag_3SeI , a trigonal $P3_1$ and a monoclinic $P2_1$ phase were also ranked among the lowest-energy structures.

We computed the lattice phonon spectrum of the experimental room-temperature cubic $Pm\bar{3}m$ phase and the five energetically most favourable structures found

| Compound | Structure | Symmetry | a (Å) | b (Å) | c (Å) | α (°) | β (°) | γ (°) | ΔE (meV/f.u.) | ΔE^{ZPE} (meV/f.u.) |
|----------------------|--------------|-------------------|---------|---------|---------|--------------|-------------|--------------|-----------------------|------------------------------------|
| Ag ₃ SCl | Cubic | $P2_13$ (I) | 7.478 | 7.478 | 7.478 | 90.000 | 90.000 | 90.000 | 0 | 0 |
| | Orthorhombic | $P2_12_12_1$ | 4.502 | 4.455 | 20.715 | 90.000 | 90.000 | 90.000 | 65 | 64 |
| | Orthorhombic | $Pca2_1$ | 5.872 | 9.757 | 6.877 | 90.000 | 90.000 | 90.000 | 79 | 78 |
| | Cubic | $P2_13$ (II) | 7.499 | 7.499 | 7.499 | 90.000 | 90.000 | 90.000 | 89 | 89 |
| | Cubic | $I2_13$ | 9.389 | 9.389 | 9.389 | 90.000 | 90.000 | 90.000 | 181 | – |
| | Cubic | $Pm\bar{3}m$ | 4.750 | 4.750 | 4.750 | 90.000 | 90.000 | 90.000 | 627 | – |
| Ag ₃ SBr | Cubic | $P2_13$ (I) | 7.586 | 7.586 | 7.586 | 90.000 | 90.000 | 90.000 | 0 | 0 |
| | Orthorhombic | $P2_12_12_1$ | 4.518 | 4.531 | 21.152 | 90.000 | 90.000 | 90.000 | 79 | 77 |
| | Cubic | $P2_13$ (II) | 7.602 | 7.602 | 7.602 | 90.000 | 90.000 | 90.000 | 91 | 90 |
| | Cubic | $I2_13$ | 9.446 | 9.446 | 9.446 | 90.000 | 90.000 | 90.000 | 117 | 109 |
| | Trigonal | $R3$ | 8.140 | 8.140 | 8.140 | 109.075 | 109.075 | 109.075 | 121 | 115 |
| | Cubic | $Pm\bar{3}m$ | 4.793 | 4.793 | 4.793 | 90.000 | 90.000 | 90.000 | 538 | – |
| Ag ₃ SI | Cubic | $P2_13$ (I) | 7.734 | 7.734 | 7.734 | 90.000 | 90.000 | 90.000 | 0 | 0 |
| | Cubic | $I2_13$ | 9.568 | 9.568 | 9.568 | 90.000 | 90.000 | 90.000 | 53 | 47 |
| | Monoclinic | $P2_1$ | 6.176 | 6.984 | 5.656 | 90.000 | 90.000 | 93.869 | 55 | 55 |
| | Cubic | $P2_13$ (II) | 7.739 | 7.739 | 7.739 | 90.000 | 90.000 | 90.000 | 67 | 73 |
| | Orthorhombic | $P2_12_12_1$ | 4.563 | 4.612 | 21.767 | 90.000 | 90.000 | 90.000 | 79 | 77 |
| | Cubic | $Pm\bar{3}m$ | 4.869 | 4.869 | 4.869 | 90.000 | 90.000 | 90.000 | 516 | – |
| Ag ₃ SeCl | Orthorhombic | $Pca2_1$ | 5.879 | 10.014 | 6.980 | 90.000 | 90.000 | 90.000 | 0 | 0 |
| | Orthorhombic | $P2_12_12_1$ (I) | 4.688 | 4.475 | 21.053 | 90.000 | 90.000 | 90.000 | 4 | 4 |
| | Orthorhombic | $P2_12_12_1$ (II) | 5.761 | 5.743 | 12.651 | 90.000 | 90.000 | 90.000 | 38 | 39 |
| | Orthorhombic | $Pna2_1$ | 6.347 | 6.450 | 9.966 | 90.000 | 90.000 | 90.000 | 43 | 38 |
| | Cubic | $I2_13$ | 9.626 | 9.626 | 9.626 | 90.000 | 90.000 | 90.000 | 117 | – |
| | Cubic | $Pm\bar{3}m$ | 4.930 | 4.930 | 4.930 | 90.000 | 90.000 | 90.000 | 1072 | – |
| Ag ₃ SeBr | Orthorhombic | $P2_12_12_1$ (I) | 4.706 | 4.562 | 21.452 | 90.000 | 90.000 | 90.000 | 0 | 0 |
| | Orthorhombic | $P2_12_12_1$ (II) | 7.530 | 14.614 | 4.365 | 90.000 | 90.000 | 90.000 | 10 | 9 |
| | Cubic | $I2_13$ | 9.678 | 9.678 | 9.678 | 90.000 | 90.000 | 90.000 | 41 | 37 |
| | Cubic | $P2_13$ (I) | 7.739 | 7.739 | 7.739 | 90.000 | 90.000 | 90.000 | 47 | 46 |
| | Cubic | $P2_13$ (II) | 7.737 | 7.737 | 7.737 | 90.000 | 90.000 | 90.000 | 49 | 48 |
| | Cubic | $Pm\bar{3}m$ | 4.962 | 4.962 | 4.962 | 90.000 | 90.000 | 90.000 | 916 | – |
| Ag ₃ SeI | Cubic | $I2_13$ | 9.782 | 9.782 | 9.782 | 90.000 | 90.000 | 90.000 | 0 | 0 |
| | Orthorhombic | $P2_12_12_1$ | 4.761 | 4.653 | 21.970 | 90.000 | 90.000 | 90.000 | 19 | 22 |
| | Trigonal | $P3_1$ | 6.949 | 6.949 | 8.388 | 90.000 | 90.000 | 120.000 | 52 | 51 |
| | Monoclinic | $P2_1$ | 7.708 | 7.225 | 15.533 | 90.000 | 90.000 | 144.418 | 66 | 70 |
| | Cubic | $P2_13$ (I) | 7.978 | 7.978 | 7.978 | 90.000 | 90.000 | 90.000 | 69 | 68 |
| | Cubic | $Pm\bar{3}m$ | 5.022 | 5.022 | 5.022 | 90.000 | 90.000 | 90.000 | 842 | – |

TABLE I. **Structural and energy properties of CAP considering several energetically competitive phases.** Energy differences, ΔE , are referred to the ground-state phase and expressed in units of meV per formula unit (f.u.). Energy differences including zero-point energy (ZPE) corrections (Methods) are also reported, ΔE^{ZPE} , except for those phases that were found to exhibit imaginary phonon frequencies. Results were obtained with the semi-local functional PBEsol [22].

for Ag₃SCl, Ag₃SeCl, Ag₃SeBr and Ag₃SeI (Supplementary Figs.3–6). Without any exception, we found that the cubic $Pm\bar{3}m$ phase always exhibits abundant imaginary phonon frequencies. The cubic $I2_13$ phase is also

vibrationally unstable for Ag₃SCl and Ag₃SeCl at low temperatures (Supplementary Figs.3–4). However, the remaining phases are perfectly vibrationally stable for all the targeted CAP (Supplementary Figs.3–6).

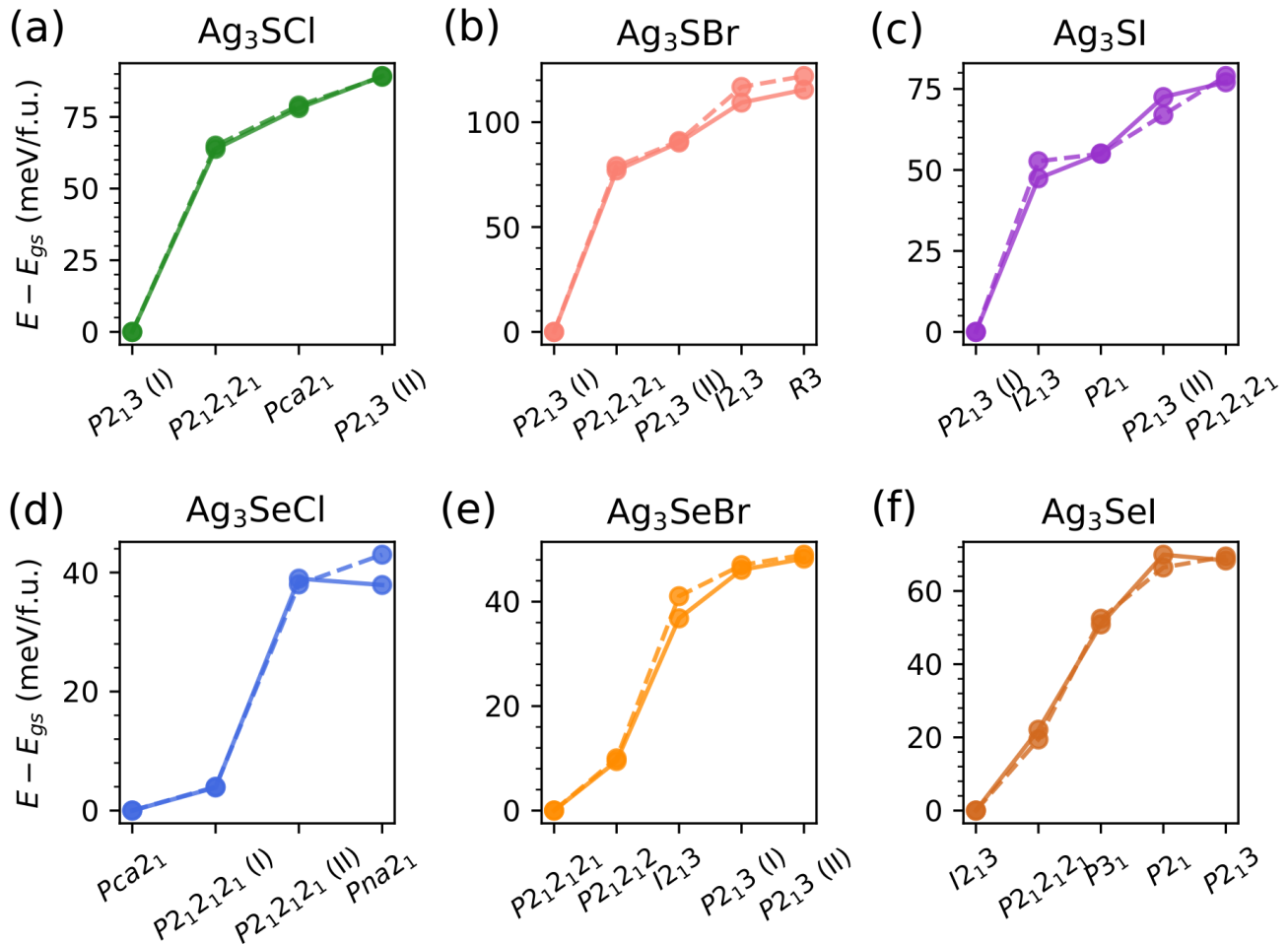


FIG. 9. **CAP phase competition determined at zero-temperature conditions.** Energy differences neglecting (including) ZPE corrections (Methods) are represented with solid (dashed) lines. Results were obtained with the semi-local functional PBEsol [22].

For the structures that exclusively exhibited real and positively defined phonon frequencies, we corrected their zero-temperature energies to account for likely quantum zero-point effects (ZPE) [27–29]. It is worth noting that applying quasi-harmonic (QH) approaches to materials that exhibit imaginary phonon frequencies is neither physically nor mathematically well-justified [27]. Thus, any QH result obtained for phases that exhibit imaginary phonon frequencies (e.g., the cubic $Pm\bar{3}m$ phase for all CAP compounds) cannot be rigorously trusted as quantitatively correct [16]. As shown in Fig.9 and Table I, accounting for quantum ZPE has a practically negligible effect on the energy rankings obtained using classical mechanics. Only in the specific cases of Ag_3SeCl and Ag_3SeI , quantum ZPE exchange the ordering between the third and fourth and the fourth and fifth most energetically favourable phases, respectively.

D. Finite-temperature phase competition

To predict likely T -induced phase transitions across the CAP family, we applied the QH free-energy formalism [27–29] to all the phases reported in Fig.9 that were vibrationally stable at low temperatures. It is worth emphasizing that applying QH approaches to phases that exhibit imaginary phonon frequencies is neither physically nor mathematically well-justified [27]. Consequently, phases like the cubic $Pm\bar{3}m$ and orthorhombic $Cmcm$ in Ag_3SbBr , for example, were excluded from our phase competition analysis conducted at $T \neq 0$ K conditions.

Figure 10 shows the QH (Helmholtz) free-energy differences estimated as a function of temperature for the six CAP compounds targeted in this study. At a given temperature, the phase exhibiting the lowest free energy (G) is the equilibrium, or stable, phase. The remaining phases, which are vibrationally stable in principle, are considered metastable. A T -induced phase transition oc-

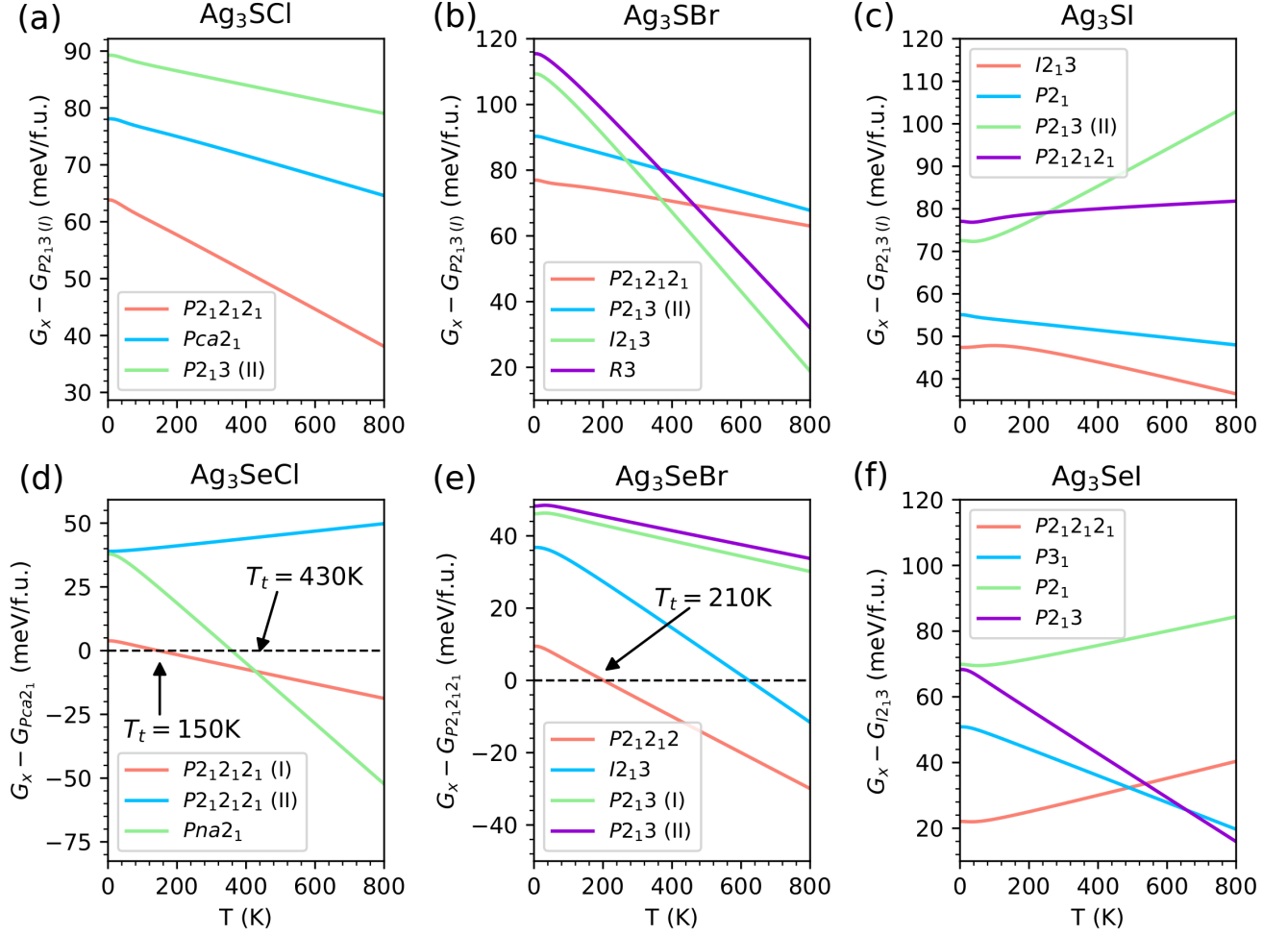


FIG. 10. **CAP phase competition determined at $T \neq 0$ conditions.** QH Helmholtz free-energy differences, ΔG , were calculated within the quasi-harmonic approximation (Methods) [27–29]. Results were obtained with the semi-local functional PBEsol [22].

curs when the free-energy curve of the equilibrium phase crosses the free-energy curve of a metastable phase. The temperature at which this crossing occurs defines the corresponding phase transition temperature.

For the S-based CAP, we did not find any T -induced phase transition up to 800 K as evidenced by the lack of G curve crossings involving the cubic $P2_13$ (I) phase. Considering higher temperatures probably is not physically meaningful due to the imminent stabilization of the liquid phase [3, 4]. Several G curve crossings involving pairs of metastable phases are observed in Figs.10b–c; however, such metastable phase transitions are not of interest in this study. Consequently, according to our QH free-energy DFT calculations, the cubic $P2_13$ (I) phase, rather than the cubic $Pm\bar{3}m$ phase, is the equilibrium, or stable, phase of Ag_3SbCl , Ag_3SbBr and Ag_3SI at room temperature.

For the Se-based CAP, the equilibrium between different phases is appreciably affected by tempera-

ture. Specifically, we predict two phase transitions for Ag_3SeCl : the first occurs between the two orthorhombic phases $Pca2_1$ and $P2_12_12_1$ (I) at 150 K, and the second between the two orthorhombic phases $P2_12_12_1$ (I) and $Pna2_1$ at 430 K (Fig.10d). For Ag_3SeBr , another phase transition is predicted to occur between the two orthorhombic phases $P2_12_12_1$ (I) and $P2_12_12_1$ (II) at 210 K (Fig.10e). Finally, for Ag_3SeI no T -induced phase transition is observed (Fig.10f). Consequently, according to our QH free-energy DFT calculations, the equilibrium room-temperature phase is orthorhombic $P2_12_12_1$ for Ag_3SeCl and Ag_3SeBr , and cubic $I2_13$ for Ag_3SeI .

III. DISCUSSION

Figure 11 shows the experimental X-ray diffraction patterns obtained for two Ag_3SbBr and Ag_3SI samples synthesized through the chemical route detailed in work

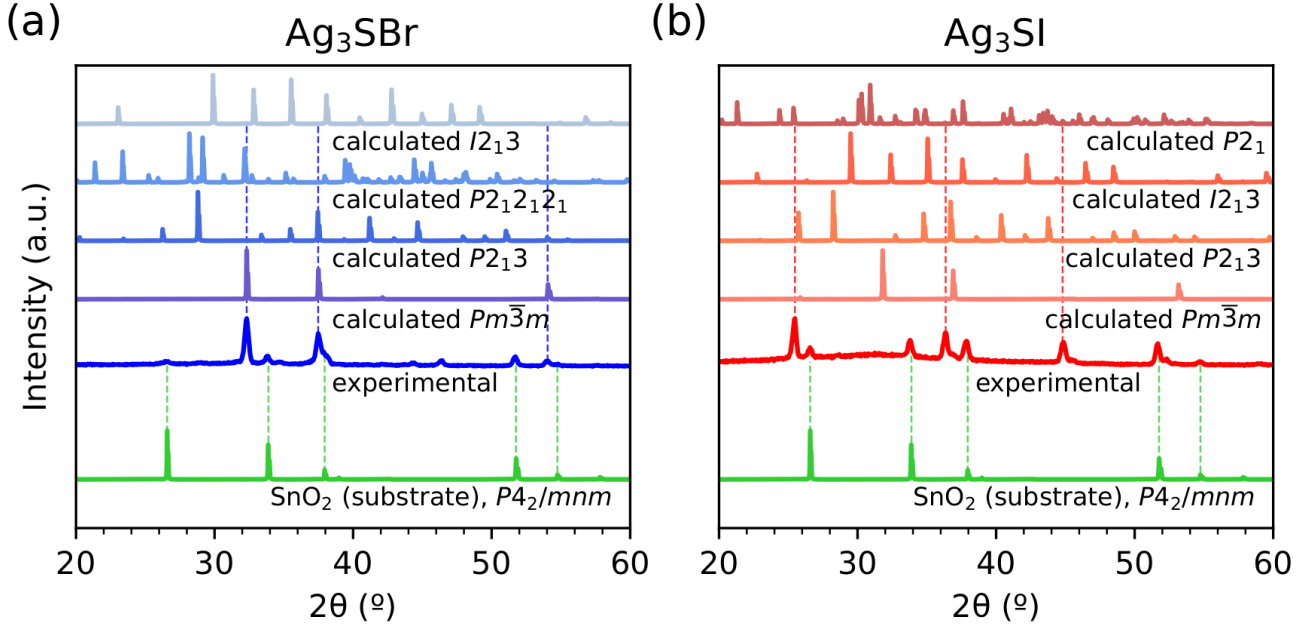


FIG. 11. **Experimental X-ray characterization of CAP at room temperature.** (a) Ag_3SBr and (b) Ag_3SI . Theoretical DFT results obtained for different energetically competitive phases are shown for comparison.

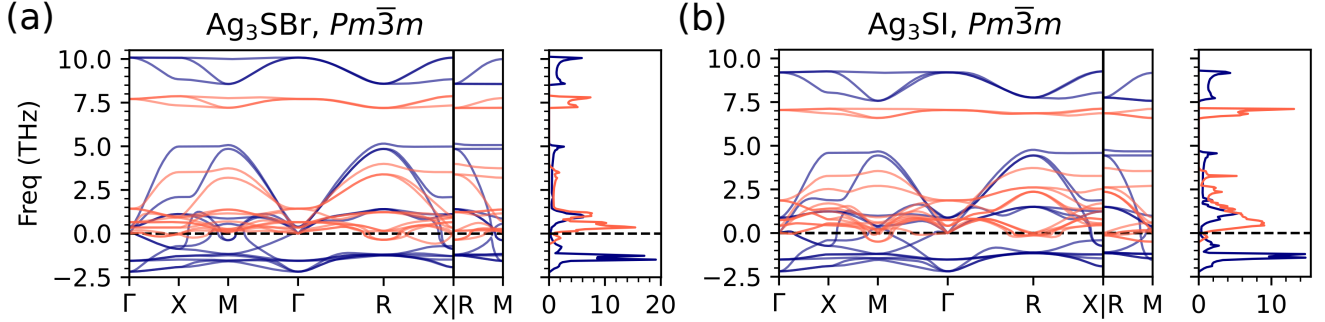


FIG. 12. **Temperature-renormalized vibrational phonon spectrum of CAP in the cubic $Pm\bar{3}m$ phase.** (a) Ag_3SBr and (b) Ag_3SI . Phonon frequencies obtained at $T = 100$ K (Methods) are represented with orange lines. Zero-temperature phonon frequencies are represented with blue lines. Results were obtained with the semi-local functional PBEsol [22].

[4] (Methods). At room temperature, based on phase identification protocols using Rietveld fits, the Ag_3SBr polycrystal was optimally indexed as cubic $Pm\bar{3}m$ and the Ag_3SI polycrystal as cubic $Im\bar{3}m$ (due to the presence of ionic disorder). In the same plot, the theoretical X-ray diffraction patterns of several phases obtained from our DFT simulations are included for comparison. The experimental X-ray diffraction pattern of the Ag_3SBr sample perfectly agrees with the theoretical X-ray diffraction pattern of the simulated cubic $Pm\bar{3}m$ phase (Fig.11a). On the other hand, the experimental X-ray diffraction pattern of the Ag_3SI sample cannot be assigned to the theoretical X-ray diffraction pattern of any single ordered structure (Fig.11b).

The experimental X-ray diffraction patterns enclosed in Fig.11, along with the computational *ab initio* findings presented in the preceding sections, raise the following question: why is the cubic $Pm\bar{3}m$ phase, or a similar disordered phase, experimentally observed in Ag_3SBr and Ag_3SI at room temperature, instead of the theoretically predicted equilibrium cubic $P2_13$ phase? Although we cannot provide a definitive answer to this question, we can offer some reasonable hypotheses.

First, it is noted that despite the cubic $Pm\bar{3}m$ phase being vibrationally unstable at very low temperatures (Figs.3–4), it could be stabilized by increasing temperature, similar to what is observed in archetypal oxide perovskites [30, 31]. To evaluate this possibility, we computed

the T -renormalized phonon spectrum of this phase for Ag_3SBr and Ag_3SI following a dynamical normal-mode-decomposition technique (Methods) [32]. Using a relatively small $2 \times 2 \times 2$ supercell for the AIMD simulations ($T = 100$ K) involved in this phonon renormalization process to maintain high numerical accuracy (Supplementary Discussion and Supplementary Fig.7), we found that the cubic $Pm\bar{3}m$ phase is practically vibrationally stabilized by thermal effects (Fig.12).

Importantly, a few imaginary phonon frequencies are still present in the T -renormalized vibrational spectra shown in Fig.12, which precluded us from estimating the QH free energy of the cubic $Pm\bar{3}m$ phase and compare it with those of other phases. It is noted that when performing T -renormalized phonon calculations at temperatures higher than 100 K, the number of imaginary phonon frequencies increased due to the appearance of ionic diffusion in the AIMD simulations. Nevertheless, despite all these technical complexities and possible numerical artifacts (Supplementary Discussion), it seems reasonable to think that the highly anharmonic cubic $Pm\bar{3}m$ phase can be fully vibrationally stabilized by effect of temperature.

Based on the presented theoretical findings, our main hypothesis is that current synthesis methods, all of which involve temperatures significantly higher than 300 K, inevitably trap CAP compounds into metastable states. A key feature, possibly explaining the room-temperature metastability of the synthesized CAP compounds, may be superionicity. According to our AIMD simulations (Supplementary Figs.8–9), Ag_3SBr in the cubic $Pm\bar{3}m$ phase becomes superionic at $T = 300$ (100) K. On other hand, the equilibrium cubic $P2_13$ phase exhibits no ionic diffusivity at room temperature. Consequently, it is likely that at temperatures higher than 300 K, such as those involved in CAP synthesis methods, the cubic $Pm\bar{3}m$ phase is further stabilized due to the entropy gain that accompanies ionic diffusion, eventually becoming the equilibrium phase. (Unfortunately, this type of entropy enhancement currently cannot be reproduced by our QH free-energy DFT calculations.) In that hypothetical case, it seems plausible that upon annealing the system becomes trapped in the cubic $Pm\bar{3}m$ phase with little possibility to nucleate the equilibrium ordered phase corresponding to lower temperatures.

IV. CONCLUSIONS

For the highly anharmonic and archetypal CAP compounds Ag_3SBr and Ag_3SI , our systematic, comprehensive and technically sound first-principles study suggest a completely different set of stable phases, both at zero temperature and $T \neq 0$ K conditions, compared to what has been proposed from experiments. Specifically, a new cubic $P2_13$ phase is found to exhibit the lowest energy at $T = 0$ K and the lowest free energy at finite temperatures, being several hundreds of meV per formula unit lower than the experimentally proposed trigonal $R\bar{3}$ and

orthorhombic $Cmcm$ phases. Additionally, we propose different ground-state phases and T -induced phase transitions for the less investigated CAP compounds Ag_3SCl , Ag_3SeCl , Ag_3SeBr and Ag_3SeI .

An interesting consequence of our theoretical findings is that the cubic $Pm\bar{3}m$ phase experimentally observed at room temperature may be metastable. The relatively high temperatures involved in current synthesis methods and the significant superionicity of CAP above room temperature may be key factors in understanding this metastability. It is worth noting that metastable phases have a natural tendency to fluctuate between different energy states, which may pose stability issues for practical technological applications. Thus, the present computational study calls for a revision of the assumed phase diagram of CAP compounds and motivates new structural characterization experiments conducted under varying temperature conditions, particularly in the low-temperature regime.

METHODS

First-principles calculations outline. *Ab initio* calculations based on density functional theory (DFT) [27] were performed to analyse the structural and phase stability properties of CAP. We performed these calculations with the VASP code [33] using different approximations to the exchange-correlation energy, namely, the semi-local functionals LDA [20], PBE [21], PBEsol [22] and SCAN [23]. The projector augmented-wave method was used to represent the ionic cores [34] and the following electronic states were considered as valence: Ag $5s\ 4d$, S $3s\ 3p$, Se $4s\ 4p$, Cl $3s\ 3p$, Br $4s\ 4p$, I $5s\ 5p$. Wave functions were represented in a plane-wave basis typically truncated at 650 eV. By using these parameters and dense \mathbf{k} -point grids for reciprocal-space integration (e.g., of $8 \times 8 \times 8$ for the cubic $Pm\bar{3}m$ phase), the resulting zero-temperature energies were converged to within 1 meV per formula unit. In the geometry relaxations, a force tolerance of $0.005\ \text{eV}\cdot\text{\AA}^{-1}$ was imposed.

Harmonic and anharmonic phonon and free-energy calculations. The second-order interatomic force constant of all CAP and resulting harmonic phonon spectrum were calculated with the finite-differences method as is implemented in the PhonoPy software [35]. Large supercells (e.g., $4 \times 4 \times 4$ for the cubic $Pm\bar{3}m$ phase containing 320 atoms) were employed for all the targeted structures. Zero-point energy (ZPE) corrections and finite-temperature Helmholtz free energies (G) were calculated within the quasi-harmonic approximation [27–29]. Due to the large number of materials and phases analyzed in this study, thermal expansion effects were disregarded in our ZPE and G calculations.

The DynaPhoPy code [32] was used to calculate the anharmonic lattice dynamics (i.e., T -renormalized phonons) of Ag_3SBr and Ag_3SI in the cubic $Pm\bar{3}m$ phase

from *ab initio* molecular dynamics (AIMD) simulations. In this case, a reduced $2 \times 2 \times 2$ supercell and $4 \times 4 \times 4$ \mathbf{k} -point grid for reciprocal-space sampling were employed in the AIMD simulations to maintain high numerical accuracy (Supplementary Discussion).

A normal-mode-decomposition technique was employed in which the atomic velocities $\mathbf{v}_{jl}(t)$ (j and l represent particle and Cartesian direction indexes) generated during fixed-temperature AIMD simulation runs were expressed like:

$$\mathbf{v}_{jl}(t) = \frac{1}{\sqrt{Nm_j}} \sum_{\mathbf{q}s} \mathbf{e}_j(\mathbf{q}, s) e^{i\mathbf{q}\mathbf{R}_{jl}^0} v_{\mathbf{q}s}(t), \quad (3)$$

where N is the number of particles, m_j the mass of particle j , $\mathbf{e}_j(\mathbf{q}, s)$ a phonon mode eigenvector (\mathbf{q} and s stand for the wave vector and phonon branch), \mathbf{R}_{jl}^0 the equilibrium position of particle j , and $v_{\mathbf{q}s}$ the velocity of the corresponding phonon quasiparticle.

The Fourier transform of the autocorrelation function of $v_{\mathbf{q}s}$ then was calculated, yielding the power spectrum:

$$G_{\mathbf{q}s}(\omega) = 2 \int_{-\infty}^{\infty} \langle v_{\mathbf{q}s}^*(0) v_{\mathbf{q}s}(t) \rangle e^{i\omega t} dt. \quad (4)$$

Finally, this power spectrum was approximated by a Lorentzian function of the form:

$$G_{\mathbf{q}s}(\omega) \approx \frac{\langle |v_{\mathbf{q}s}|^2 \rangle}{\frac{1}{2} \gamma_{\mathbf{q}s} \pi \left[1 + \left(\frac{\omega - \omega_{\mathbf{q}s}}{\frac{1}{2} \gamma_{\mathbf{q}s}} \right)^2 \right]}, \quad (5)$$

from which a T -renormalized quasiparticle phonon frequency, $\omega_{\mathbf{q}s}(T)$, was determined as the peak position, and the corresponding phonon linewidth, $\gamma_{\mathbf{q}s}(T)$, as the full width at half maximum.

First-principles molecular dynamics simulations. *Ab initio* molecular dynamics simulations based on DFT were performed in the canonical (N, V, T) ensemble (i.e., constant number of particles, volume and temperature). The selected volumes were those determined at zero temperature hence thermal expansion effects were neglected. The temperature in the AIMD simulations was kept fluctuating around a set-point value by using Nose-Hoover thermostats. Large simulation boxes containing $N \sim 200$ –400 atoms were employed (e.g., for the cubic $Pm\bar{3}m$ phase we adopted a $4 \times 4 \times 4$ supercell containing 320 atoms) and periodic boundary conditions were applied along the three supercell lattice vectors. Newton's equations of motion were integrated using the customary Verlet's algorithm with a time step of $1.5 \cdot 10^{-3}$ ps. Γ -point

sampling for reciprocal-space integration was employed in most of the AIMD simulations, which comprised long simulation times of 80–100 ps.

Crystal structure searches. We used the MAGUS software (Machine learning And Graph theory assisted Universal structure Searcher) [19] to find new candidate stable and metastable phases for the archetypal CAP Ag_3SBr and Ag_3SI . This crystal structure prediction software employs an evolutionary algorithm augmented with machine learning and graph theory to reduce the cost of the geometry optimizations. The crystal phase searches were conducted for structures containing a maximum of 4 formula units (i.e., 20 atoms per unit cell).

Experimental procedure. Ag_3SBr and Ag_3SI were synthesized following the chemical route described in work [4]. The samples were analyzed through X-ray diffraction using a Bruker D8 advanced diffractometer equipped with a Cu-based tube (40 kV, 40 mA) and a Sol-X detector with discriminator for the K_β line and fluorescence effect reduction. The measurements were made using grazing incidence configuration.

DATA AVAILABILITY

The data that support the findings of this study are freely available at the NOMAD data management platform for materials science [36]. These data include the VASP input files of our first-principles DFT calculations as well as some key output files (e.g., relaxed atomic positions of all relevant crystal structures) [37].

ACKNOWLEDGEMENTS

C.C. acknowledges support from the Spanish Ministry of Science, Innovation and Universities under the fellowship RYC2018-024947-I and grants PID2020-112975GB-I00 and grant TED2021-130265B-C22. The authors also thankfully acknowledge technical support the computational resources at MareNostrum4 provided by Barcelona Supercomputing Center (FI-2023-1-0002, FI-2023-2-0004, FI-2023-3-0004 and FI-2024-1-0005). P.B. acknowledges support from the Generalitat de Catalunya under a FI grant. C.L. acknowledges support from the Spanish Ministry of Science, Innovation and Universities under a FPU grant.

[1] Palazon, F. Metal chalcogenides: Next generation photovoltaic materials? *Sol. RRL* **6**, 2100829 (2022).

[2] Ghorpade, U.V., Suryawanshi, M. P., Green, M. A., Wu, T., Hao, X. and Ryan, K. M. Emerging chalcogenide

- materials for energy applications. *Chem. Rev.* **123**, 327 (2023).
- [3] Sebastia-Luna, L., Rodkey, N., Mirza, A. S., Mertens, S., Lal, Melchor, A., Carranza, G., Calbo, J., Righetto, M., Sessolo, M., Herz, L. M., Vandewal, K., Ortı, E., Morales-Masis, M., Bolink, H. J. and Palazon, F. Chalcogenide antiperovskite thin films with visible light absorption and high charge-carrier mobility processed by solvent-free and low-temperature methods. *Chem. Mater.* **35**, 6482 (2023).
- [4] Cano, I., Turnley, J. W., Benıtez, P., Lopez-Alvarez, C., Asensi, J.-M., Payno, D., Puigdollers, J., Placidi, M., Cazorla, C., Agrawal, R. and Saucedo, E. Novel synthesis of semiconductor chalcogenide anti-perovskites by low-temperature molecular precursor ink deposition methodologies. *J. Chem. Mater. C* **12**, 3154 (2024).
- [5] Takahashi, T. and Yamamoto, O. The Ag/Ag₃SI/I₂ solid-electrolyte cell. *Electrochim. Acta* **11**, 779 (1966).
- [6] Hull, S. Superionics: crystal structures and conduction processes. *Rep. Prog. Phys.* **67**, 1233 (2004).
- [7] Wakamura, K., Miura, F., Kojima, A. and Kanashiro, T. Observation of anomalously increasing phonon damping constant in the β phase of the fast-ionic conductor Ag₃SI. *Phys. Rev. B* **41**, 2758 (1990).
- [8] Sakuma, T. Treatment of anharmonic thermal vibration by using transformation of scattering vector. *J. Phys. Soc. Jpn.* **54**, 4188 (1985).
- [9] Kawamura, J., Shimoji, M. and Hoshino, H. The ionic conductivity and thermoelectric power of the superionic conductor Ag₃SBr. *J. Phys. Soc. Jpn.* **50**, 194 (1981).
- [10] Magistris, A., Pezzati, E. and Sinistri, C. Thermoelectric properties of high-conductivity solid electrolytes. *Z. Naturforsch.* **27a**, 1379 (1972).
- [11] Reuter, B. and Hardel, K. Silbersulfidbromid und silbersulfidjodid. *Angew. Chem.* **72**, 138 (1960).
- [12] Hoshino, S., Sakuma, T. and Fujii, Y. The existence of the order phase in superionic conductor Ag₃SI. *J. Phys. Soc. Jpn.* **45**, 705 (1978).
- [13] Sakuma, T. and Hoshino, S. The phase transition and the structures of superionic conductor Ag₃SBr. *J. Phys. Soc. Jpn.* **49**, 678 (1980).
- [14] Hoshino, S., Fujishita, H., Takashige, M. and Sakuma, T. Phase transition of Ag₃SX (X= I, Br). *Solid State Ion.* **3**, 35 (1981).
- [15] Cho, N., Kikkawa, S., Kanamaru, F. and Yoshiasa, A. Structural refinement of Ag₃SI by single crystal X-ray diffraction method. *Solid State Ion.* **68**, 57 (1994).
- [16] Yin, L., Murphy, M., Kim, K., Hu, L., Cabana, J., Siegel, D. J. and Lapidus, S. H. Synthesis of antiperovskite solid electrolytes: comparing Li₃SI, Na₃SI, and Ag₃SI. *Inorg. Chem.* **59**, 11244 (2020).
- [17] Honda, H., Basar, K., Siagian, S., Sakuma, T., Takahashi, H., Kawaji, H. and Atake, T. Low-temperature phase in superionic conductor Ag₃SBr_xI_{1-x}. *J. Phys. Soc. Jpn.* **76**, 114603 (2007).
- [18] Shahrokhi, S., Dubajic, M., Dai, Z.-Z., Bhattacharyya, S., Mole, R. A., Rule, K. C., Bhadhbade, M., Tian, R., Mussakhanuly, N., Guan, X., Yin, Y., Nielsen, M. P., Hu, L., Lin, C.-H., Chang, S. L. Y., Wang, D., Kabakova, I. V., Conibeer, G., Bremner, S., Li, X.-Y., Cazorla, C. and Wu, T. Anomalous structural evolution and glassy lattice in mixed-halide hybrid perovskites. *Small* **18**, 2200847 (2022).
- [19] Wang, J., Gao, H., Han, Y., Ding, C., Pan, S., Wang, Y., Jia, Q., Wang, H.-T., Xing, D. and Sun, J. MAGUS: machine learning and graph theory assisted universal structure searcher. *Nat. Sci. Rev.* **10**, nwad128 (2023).
- [20] Ceperley, D. M. and Alder, B. J. Ground state of the electron gas by a stochastic method. *Phys. Rev. Lett.* **45**, 566 (1980).
- [21] Perdew, J. P., Burke, K. and Ernzerhof, M. Generalized gradient approximation made simple. *Phys. Rev. Lett.* **77**, 3865 (1996).
- [22] Perdew, J. P., Ruzsinszky, A., Csonka, G. I., Vydrov, O. A., Scuseria, G. E., Constantin, L. A., Zhou, X. and Burke, K. Restoring the density-gradient expansion for exchange in solids and surfaces. *Phys. Rev. Lett.* **100**, 136406 (2008).
- [23] Sun, J., Ruzsinszky, A. and Perdew, J. P. Strongly constrained and appropriately normed semilocal density functional. *Phys. Rev. Lett.* **115**, 036402 (2015).
- [24] Cazorla, C., D. Alfe and Gillan, M. J. Constraints on the phase diagram of molybdenum from first-principles free-energy calculations. *Phys. Rev. B* **85**, 064113 (2012).
- [25] Cazorla, C. and Errandonea, D. Superionicity and polymorphism in calcium fluoride at high pressure. *Phys. Rev. Lett.* **113**, 235902 (2014).
- [26] Stokes, H. T. and Hatch, D. M. FINDSYM: program for identifying the space-group symmetry of a crystal. *J. Appl. Cryst.* **38**, 237 (2005).
- [27] Cazorla, C. and Boronat, J. Simulation and understanding of atomic and molecular quantum crystals. *Rev. Mod. Phys.* **89**, 035003 (2017).
- [28] Cazorla, C., Errandonea, D. and Sola, E. High-pressure phases, vibrational properties, and electronic structure of Ne(He)₂ and Ar(He)₂: A first-principles study. *Phys. Rev. B* **80**, 064105 (2009).
- [29] Cazorla, C. and Rurali, R. Dynamical tuning of the thermal conductivity via magnetophononic effects. *Phys. Rev. B* **105**, 104401 (2022).
- [30] Ehsan, S., Arrigoni, M., Madsen, G. K. H., Blaha, P. and Troster, A. First-principles self-consistent phonon approach to the study of the vibrational properties and structural phase transition of BaTiO₃. *Phys. Rev. B* **103**, 094108 (2022).
- [31] Cazorla, C., Bichelmaier, S., Escorihuela-Sayalero, C., Iniguez J., Carrete, J. and Rurali, R. Light-driven dynamical tuning of the thermal conductivity in ferroelectrics. *Nanoscale* **16**, 8335 (2024).
- [32] Carreras, A., Togo, A. and Tanaka, I. DynaPhoPy: A code for extracting phonon quasiparticles from molecular dynamics simulations. *Comput. Phys. Commun.* **221**, 221 (2017).
- [33] Kresse, G. and Furthmuller, J. Efficient iterative schemes for *ab initio* total-energy calculations using a plane-wave basis set. *Phys. Rev. B* **54**, 11169 (1996).
- [34] Blochl, P. E. Projector augmented-wave method. *Phys. Rev. B* **50**, 17953 (1994).
- [35] Togo, A. and Tanaka, I. First principles phonon calculations in materials science. *Scr. Mater.* **108**, 1 (2015).
- [36] Scheidgen, M., Himanen, L., Ladines, A. N. *et al.* NOMAD: A distributed web-based platform for managing materials science research data. *J. Open Source Softw.* **8**, 5388 (2023).
- [37] DOI:10.17172/NOMAD/2024.05.17-2